The morphology and phase mixing studies on poly(ester–urethane) during shape memory cycle

I. M. Pereira · R. L. Oréfice

Abstract Three series of shape memory poly(ester–urethane) with varying hard-segment contents were synthesized. The materials were designed to display a three-phase structure consisting of a disperse phase formed by crystallites and hard domains embedded in an amorphous matrix. The initial undeformed morphology was investigated using techniques such as modulated differential scanning calorimetry, Fourier transform infrared spectroscopy, and wide angle X-ray scattering. These techniques were used to determine the phase separation, hydrogen-bonding structure, and crystalline fraction of the specimens prior to thermo-mechanical treatments. The obtained information was correlated with small angle X-ray scattering investigations of morphological changes that occurred during shape memory cycling. The deformation cycle led to the formation of an oriented nanostructure derived from chain alignment. The nanostructure recovered was observed to be triggered by the melting of the crystallites and bulk incompatibility. A relationship between the ability of the studied poly(ester–urethane) specimens to recover their original shape and their original nanostructure was determined.

I. M. Pereira
Federal Center of Technological Education of Minas Gerais,
Timoteo, Brazil
e-mail: iacipere@yahoo.com.br

I. M. Pereira
Department of Metallurgy, Av. Amazonas 1193, Vale Verde,
35.180-000 Timóteo, Minas Gerais, Brazil

R. L. Oréfice (✉)
Department of Metallurgical and Materials Engineering,
Federal University of Minas Gerais, Rua Espírito Santo 35, s206,
Centro, 30.160-030 Belo Horizonte, Minas Gerais, Brazil
e-mail: rorefice@demet.ufmg.br

Introduction

Polyurethanes (PUs) are an important class of special polymers that comprise a diverse family [1]. Linear segmented thermoplastic PU elastomers are PUs characterized by having a chain backbone arranged as a block copolymer. The properties of these materials are dependent on the two- or polyphase morphology. On the other hand, the morphology and structure are dependent on the chemical composition and the length of the segments, among other factors. In general, segmented PUs have soft and hard segments. The soft segments display high mobility, are usually presented in a coiled conformation, and alternate with units of hard segments [2]. Due to incompatibility between the hard and soft segments, segmented PU elastomers can undergo phase separation on a microscale, forming hard and soft domains [3, 4]. Recent approaches have tailored PU properties to yield thermo-responsive materials, described as shape memory polymers (SMPs), with the ability to remember a permanent shape that can substantially differ from an initial temporary shape [5]. In general, SMPs can be thought of as materials with morphologies consisting of two phases: a shape-fixing matrix phase and a shape-memorizing dispersed phase. Beyond the actuation transition of the shape-fixing phase, the polymer can be deformed from its primary shape to a secondary shape by the application of stress, and it can then be locked into the secondary shape by cooling to below the actuation transition temperature [6]. The efficiency of a SMP is empirically controlled by the polymer's chemical structure, molecular weight, degree of cross-linking, and fraction of amorphous and crystalline domains [7].

Although some research in this field has been carried out [8, 9], the details of the morphological changes that occur during shape memory cycling are still poorly understood,

mainly because segmented PUs exhibit a complex phase structure that depends on the type and size of the segments used as well as on the processing conditions. Furthermore, these features impact not only shape memory properties, but also physical properties as well. Hence, understanding the correlations between chemical and morphological structures and shape memory properties is essential in designing SMPs for practical applications.

This study aims to identify the role of the chemical and morphological structures of PUs during shape memory cycling. Differential scanning calorimetry (DSC), wide angle X-ray scattering (WAXS), and Fourier transform infrared spectroscopy (FTIR) were used to study the morphological features. Additionally, the mechanical and shape memory properties were determined and are discussed in relation to the results obtained by WAXS and FTIR. Finally, SAXS measurements were carried out to investigate the structural changes that occur during shape memory cycling.

Materials and methods

Materials

Poly(caprolactone diol) (PCL M_n = 530, 10,000 g mol^{-1}), isophorone diisocyanate (IPDI), 2,2-bis(hydroxymethyl) propionic acid (DMPA), and dibutyl tin dilaurate (DBDLT) were obtained from Aldrich. Triethylamine (TEA, 98%) and hydrazine (HZ, 25%) were purchased from Vetec. All of these chemicals were employed throughout this work without any previous treatment.

Prepolymer synthesis

PUs were prepared via a prepolymer mixing method using a 250-mL three-neck glass flask equipped with a heating mantel, a mechanical stirrer, and a thermometer. The PCL and DMPA were stirred in the glass reactor at 65 °C for 30 min. IPDI was added to the reactor in the presence of DBDLT (NCO/OH ratio of 2) under a N$_2$ atmosphere. The reaction was carried out at 70–75 °C for 3 h.

Neutralization of the prepolymer

After cooling to 40 °C, the prepolymer and the carboxylic acid groups were neutralized by the addition of TEA. The mixture was then gently stirred for 40 min.

Dispersion and chain extension

Water dispersion and PU chain extension were achieved by adding HZ and deionized water to the neutralized prepolymer under high-speed stirring. To ensure that the

Table 1 Composition (wt%) of waterborne PUs

Sample	PCL (%)		DMPA	IPDI	HZ (100%)	TEA
	530	10,000				
PU-I	18.78	–	3.59	27.63	1.99	2.70
PU-II	5.59	56.82	1.64	12.66	0.91	1.24
PU-III	–	64.33	0.65	5.02	0.36	0.49

reaction was complete, the mixture was stirred for 30 min. This chemical procedure was successful in producing PU water dispersions with a solid content of about 30% (PUs). The feed ratios are shown in Table 1.

W(HS) is the weight fraction of the hard segment, obtained according to Eq. 1:

$$W(\mathrm{HS}) = \frac{\mathrm{Weight_{IPDI}} + \mathrm{Weight_{HZ}}}{\mathrm{Weight_{PU}}} \times 100 \qquad (1)$$

Film formation

Films were produced by casting the dispersions in a PVC mold and allowing them to dry at 17 °C for 1 week. The films were then annealed at 80 °C for 72 h.

Infrared spectroscopy

Infrared spectra were collected at room temperature in a Fourier transform infrared spectrophotometer (FTIR; Perkin–Elmer, model Spectrum 1000). Measurements were carried out using the attenuated total reflectance technique. Each spectrum represents 64 scans with a resolution of 4 cm^{-1}.

Wide angle X-ray scattering

WAXS analysis was performed on samples with a thickness of 0.8–1.0 mm and a diameter of 14 mm, using a Philips model PW1710 diffractometer operated with Cu K_α irradiation at a scan rate of 2° 2θ/s in the range of 5–60°.

Thermal analysis

Modulated DSC measurements were performed using a TA Instruments 2920. The following protocol was applied to each sample: (1) heat from room temperature to 110 °C at 15 °C min^{-1}, (2) hold for 3.00 min at 110 °C, (3) cool to −110 °C at 3.00 °C/min, modulating ±1.00 °C every 60 s, (4) hold for 3.00 min at −110 °C, and (5) heat again to 110 °C at 3.00 °C/min, modulating ±1.00 °C every 60 s. Data were collected from the first cooling and the second heating. The melting and re-crystallization temperatures were taken as peak maxima; the glass transition temperature (T_g) and the enthalpies of the melting peaks were obtained by the analysis software of the calorimeter.

Mechanical properties

The tensile strength (σ_m), initial modulus (E), and elongation at break (ε_m) of the samples (DIN60) were measured using a universal testing machine (DL3000, EMIC) at a crosshead speed of 10 mm/min. The sample length between the clamps was 20 mm. The tests were performed at room temperature.

Shape memory properties

Shape memory experiments were done using a universal testing machine (DL3000, EMIC) with a constant temperature heating device. The specimens were heated using a fluorescent lamp and were cooled by cold water. A thermocouple was attached to the specimen in order to control its temperature. The specimens were deformed at a crosshead speed of 10 mm/min. Scheme 1 illustrates the heating and cooling system.

The shape recovery cycle consisted of the following steps: (1) the samples were deformed to a defined strain, L_m, at 80 °C. (2) While maintaining the strain at L_m, the samples were cooled to room temperature. (3) Mechanical constraints on the polymers were removed. (4) The samples were subsequently heated to 80 °C in an oven and were kept at this temperature for l5 min to recover their original shape. This completes one thermomechanical cycle, leaving a residual strain. Scheme 2 illustrates the shape-memory thermomechanical cycle test.
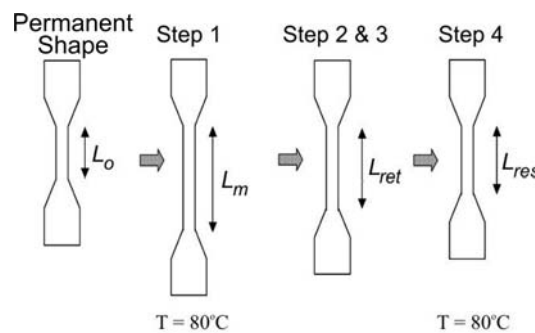
The loading stage of the thermomechanical cycle test defines a stress–strain curve. The SM properties of the materials were described by the strain recovery ratio, R_R, and the strain fixity ratio, R_f. Both can be determined by Eqs. 2 and 3:

$$R_r(\%) = \frac{L_m - L_{Res}}{L_m - L_o} \times 100, \tag{2}$$

$$R_f(\%) = \frac{L_{Ret} - L_o}{L_m - L_o} \times 100, \tag{3}$$
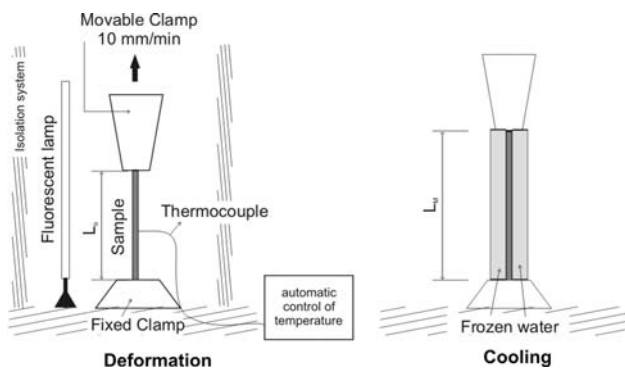
Scheme 1 Shape memory test set-ups

Scheme 2 Thermomechanical shape memory cycle

where L_o is the original length, L_m is the deformed length, L_{ret} is the retained length, and L_{res} is the length after recovery. Values of L_m close to 22 mm were used.

Synchrotron small angle X-ray scattering

Synchrotron small angle X-ray scattering (SAXS) measurements were performed using the beam line of the National Synchrotron Light Laboratory (LNLS, Campinas, Brazil). After passing through a thin beryllium window, the beam is monochromatized ($\lambda = 1.488$ Å) and horizontally focused by a cylindrically bent and asymmetrically cut silicon single crystal. The X-ray scattering intensity, $I_{(q)}$, was experimentally determined as a function of the scattering vector, q, whose modulus is given by Eq. 4:

$$q = \frac{4\pi}{\lambda} \sin\theta, \tag{4}$$

where λ is the X-ray wavelength and θ is half the scattering angle. Each SAXS pattern corresponds to a data collection time of 900 s. From the experimental scattering intensity produced by all of the studied samples, the parasitic scattering intensity produced by the collimating slits was subtracted. All SAXS patterns were corrected for the nonconstant sensitivity of the position sensitive X-ray detector, for the time-varying intensity of the direct synchrotron beam, and for differences in sample thickness. Due to the normalization procedure used, the SAXS intensity was determined for all samples in the same arbitrary units to allow for direct comparison. A sample-detector distance of 551.6 mm was used during the measurements.

Results and discussion

Thermal analysis

The thermal behavior of the obtained PUs is shown in Fig. 1a during cooling and in Fig. 1b during the second heating. The thermal properties are summarized in Table 2.
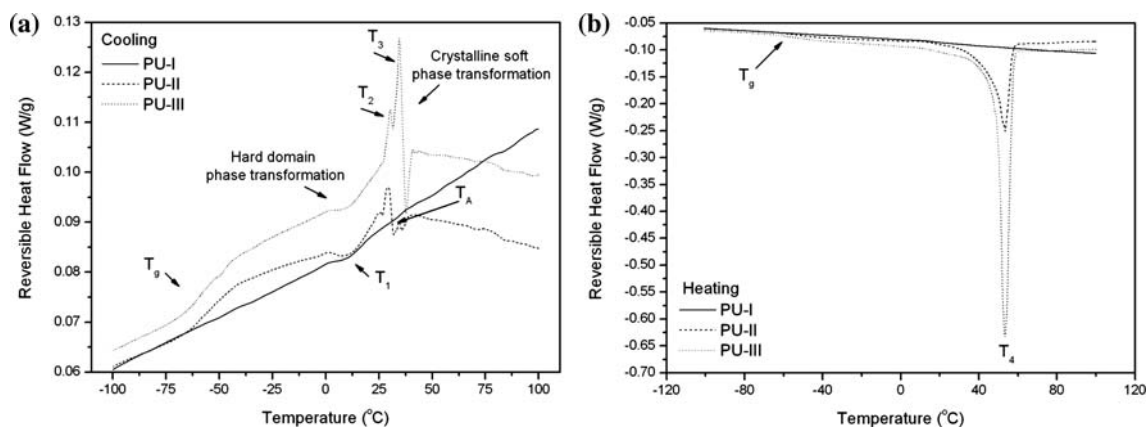
Fig. 1 DSC curves for the obtained PUs: **a** cooling and **b** heating

Table 2 DSC results of the obtained poly(ester–urethane) specimens

	T_g (°C)	T_{onset} (°C)	T_{end} (°C)	Zone width	T_1 (°C)	T_2 (°C)	T_A (°C)	T_3 (°C)	T_4 (°C)	C_P (J/g)
PU-I	–	–	–	–	8.9	–	–	–	–	–
PU-II	−57.7	−64.7	−45.5	19.1	7.7	24.8	28.9	34.6	53.5	127.8
PU-III	−60.2	−64.1	−53.1	11.0	8.4	30.4	–	34.6	53.3	179.0

High molecular weight PCL has a second-order glass transition at −60 °C, a first-order transition at 69.8 °C corresponding to a melting endotherm, an exothermic crystallization peak around 25 °C, and a crystallization heat of 16.9 kJ mol^{-1} [10, 11].

In DSC analysis, the width of a transition zone provides a qualitative measure of phase homogeneity, and the variation in the magnitude of T_g can indicate the degree of microphase separation [12]. In the cooling run, shown in Fig. 1a, a glass transition is observed for PU-II and PU-III around −60 °C. Based on the T_g data, given in Table 2, the PU-II glass transition temperature is found to be higher than that of PU-III. This means that a larger amount of hard segments dissolves in the PU-II soft-segment matrix, resulting in an increase in the soft-segment glass transition temperature. In addition to the increase in the T_g values, a broadening of the width of the transition zone is observed, also suggesting a higher degree of phase mixture in PU-II. All of the obtained PUs showed an endothermic inflection centered at T_1 associated with the hard-segment domain. According to Seymour and Cooper [13], the endotherm region observed in the DSC data for PUs may be ascribed to a morphological effect, and it is a function of the hard-segment length. Clusters of shorter hard segments give rise to lower temperature endotherms [12, 13]. Upon cooling, PU-II and PU-III recrystallized to a certain extent. During recrystallization, PU-II displayed three exothermic peaks, T_2, T_3, and T_A, while PU-III displayed only two, T_2 and T_3.

This difference could be due to the differing crystal structures of PU-II and PU-III.

During the second heating, PU-I showed a smooth baseline, whereas PU-II and PU-III showed a glass transition and an endothermic inflection centered at T_4, assigned to melting of the crystalline soft-segment phase. The endotherm maxima were observed below the value of 69.8 °C given for pure high molecular weight PCL. This reduction could be due to the mixing of the hard phase and/or to imperfections in the crystal packing. Hence, the phase mixture not only disturbs crystallization, reducing the crystal fraction, but also promotes the formation of less perfect crystals, which require less energy to melt. The data evidences the complex phase morphology of the obtained PUs, in which the soft segment forms a continuous matrix, with a glass transition temperature around −60 °C, with a disperse phase consisting of poorly ordered hard microregions, possibly containing ionic groups, and well-ordered but imperfect crystallites.

Infrared spectroscopy

Typical infrared spectra of PU-I, PU-II, and PU-III, which have compositions defined in Table 1, are shown in Fig. 2. The characteristic bands of poly(ester–urethane) are marked in Fig. 2 and described in Table 3, where the band frequency and the correspondent functional groups are shown [14–21].
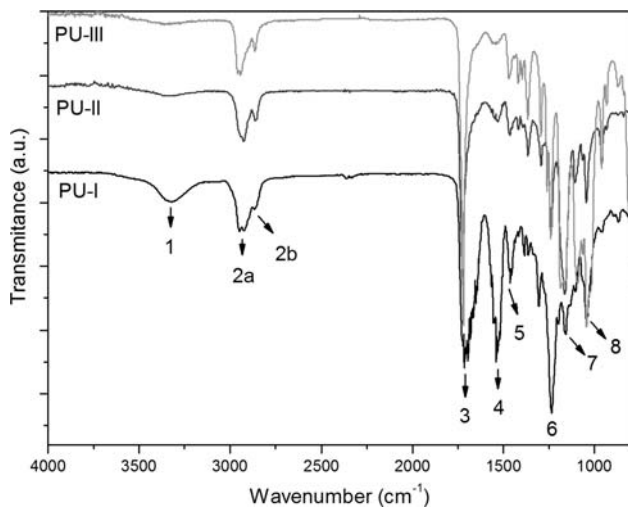
Fig. 2 FTIR spectra of PU-I, PU-II, and PU-III

Hydrogen bonding is known to be an important driving force for phase separation of a hard segment from a soft-segment matrix. Two main spectral regions are of interest in studying the hydrogen bonding of segmented PUs: N–H and C=O, respectively, primary amine stretching and carbonyl group stretching. As band overlapping occurs at bands 1 and 3, a deconvolution mathematical procedure (by using PickFiT® software) was performed for the spectra shown in Fig. 2. Figure 3a and b illustrates, respectively, the deconvolution procedure used to determine the overlapped bands 1 and 3 of the FTIR spectrum of the obtained PUs.

The N–H bands of PU-I and PU-II demonstrate that the NH is nearly completely hydrogen bonded. The ratio

between the band areas shows, respectively, that 97% and 86% of the NH groups are hydrogen bonded. The NH of PU-III, however, is only 64% hydrogen bonded.

The extent to which the carbonyl absorption groups participate in hydrogen bonding can be expressed by a hydrogen-bonding index HBI(%), which is the fraction of hydrogen bonding in the carbonyl group stretching vibrations (Eq. 5) [18, 22–24].

$$HBI(\%) = \frac{A_{1700} + A_{1640}}{A_{1700} + A_{1640} + A_{1724} + A_{1660}} \times 100, \quad (5)$$

where A_{1724}, A_{1700}, A_{1660}, and A_{1640} are, respectively, the FTIR absorption band area of free urethane, bonded urethane, free urea, and bonded urea.

The microphase separation structure of PUs depends on many factors, i.e., the structure and molecular weight of the soft segment, the nature of the chain extender, the hard-segment content and interactions, and the thermal and solvent history during sample preparation [25]. The multiphase structure of PUs was first proposed by Cooper and Tobolsky [26] and is a result of the repulsive interaction between dissimilar segments and the thermodynamic immiscibility of hard and soft segments at low temperatures [26–28].

The PU-I, PU-II, and PU-III HBI(%) results are, respectively, 52.1%, 39.8%, and 29.8%. The DSC results predict that the degree of phase mixing follows the order of PU-I > PU-II > PU-III. The highly hydrogen-bonded hard segments of PU-I act as physical cross links, restricting segmental motion of the polymer chain. However, this does not result in a more significant phase separation between the hard and soft segments because the weight fraction of

Table 3 Origin, group frequency, and functional group of the spectral bands observed in Fig. 2

| Item	Origin	Group frequency wavenumber (cm^{-1})	Assignment
1	N–H	3600–3150	Primary amine stretching modes
		∼3500	Free N–H stretching band
		∼3300	Hydrogen-bonded N–H band
2	–CH₃	3000–2800	Methylene groups stretching modes
			2A–Asymmetric mode
			2B–Symmetric mode
3	C=O	1760–1600	Carbonyl groups stretching vibrations
		1750–1725	Ester stretching modes
		∼1720	Free urethane stretching band
		∼1700	Hydrogen-bonded urethane stretching band
		∼1660	Free urea stretching band
		∼1630	Hydrogen-bonded urea stretching band
4	>N–H	1640–1540	Secondary amide modes
5	–CH₃	1470–1430	Methylene groups asymmetric bend modes
6	C–N	1292–1226	Tertiary amide stretching modes
7	C–O–C	∼1150	Ether stretching vibration
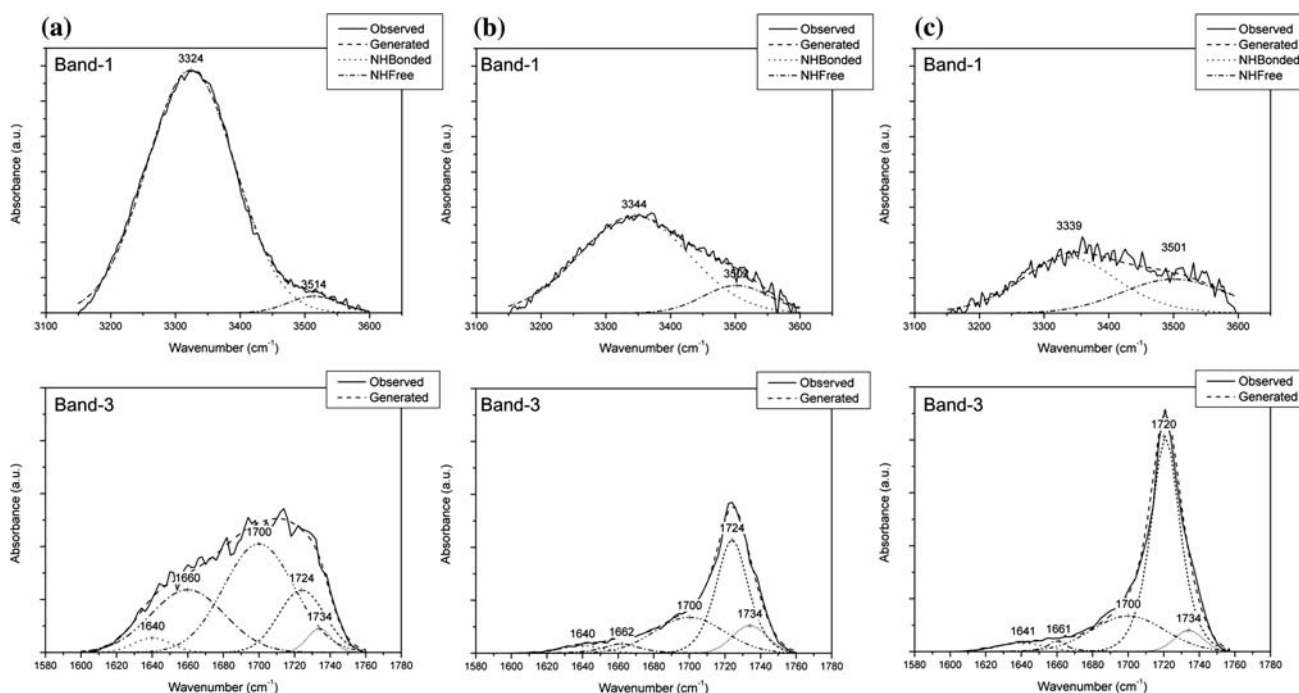
Fig. 3 Deconvoluted FTIR spectrum, Band-1 and Band-3, of samples: (**a**) PU-I, (**b**) PU-II and (**c**) PU-III

the hard segment in PU-I is three times larger than that of PU-II and seven times larger than that of PU-III. On the other hand, the lower HBI(%)values for PU-II and PU-III do not result in more extensive phase mixing due to their lower weight fraction of hard segments. Moreover, looser, and longer polymer chains are more likely to realign and crystallize, increasing the phase separation. Some previous works [29–31] have not considered the effect of the hard-segment content on the phase separation. Nevertheless, the HBI(%) values alone were not able to predict the phase separation structure of the obtained PUs.

Wide angle X-ray scattering

Figure 4 shows the WAXS profiles of the PUs and PCL10000. The diffraction curve of PU-I has a broad shoulder around $2\theta = 20°$, which is typical of a noncrystalline state with a characteristic small-scale order (interchain spacing) of 0.4–0.5 nm [32–34]. The diffraction patterns of PU-II and PU-III are typical of semi-crystalline polymers. In PU containing only PCL 530 (i.e., PU-I), the fraction of hard segments is high enough to restrict PCL crystallization, and the high levels of hydrogen bonding, observed through the FTIR results, also contribute to the stabilization of the amorphous structure.

The amorphous and crystalline parts of PCL10000, PU-II, and PU-III were separated by a deconvolution procedure using PickFiT® software. Gaussian curves were used to describe the amorphous phase and the crystalline
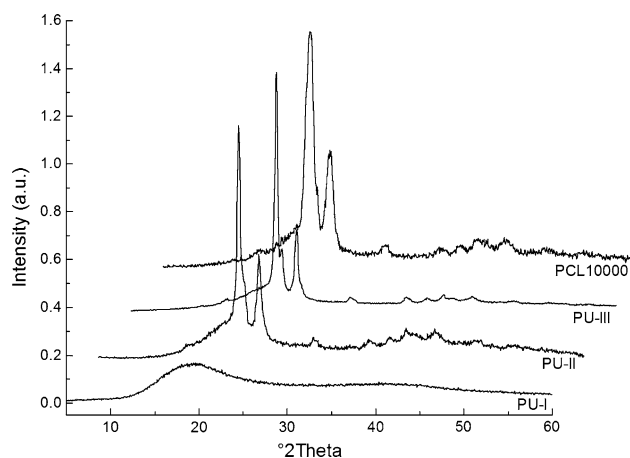

Fig. 4 WAXS pattern of the obtained poly(ester–urethane) and PCL10000

reflections. The crystalline peaks were established according to the WAXS scattering results. The experimental WAXS results and the deconvoluted separated curves are given in Fig. 5.

The crystallinity index, α_X, is defined as the ratio of the area under the separate crystalline pattern ($\sum A_{crystalline}$) and the total scattering, $\sum A_{crystalline} + \sum A_{amorphous}$, of the original pattern, according to Eq. 6 [26, 35]:

$$\alpha_X = \left[\frac{\sum A_{crystalline}}{\left(\sum A_{crystalline} + \sum A_{amourphous} \right)} \right] \times 100. \tag{6}$$
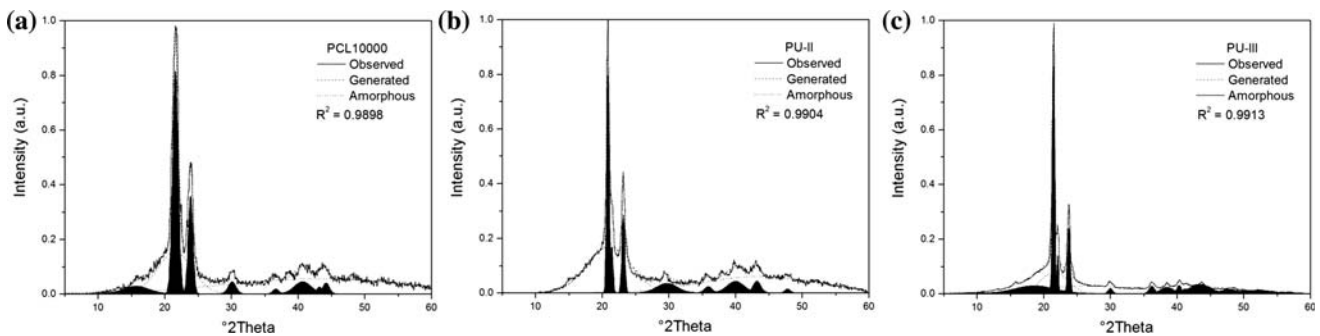
Fig. 5 Experimental WAXS curves and their separation into amorphous and crystalline parts: **a** PCL10000, **b** PU-II, and **c** PU-III

The PU-II, PU-III, and PCL10000 crystallinity indexes are, respectively, 27.1%, 54.9%, and 34.5%.

Synchrotron small angle X-ray scattering

In this work, SAXS techniques were used to gather information regarding the effect of the poly(ester–urethane) macromolecular architecture on the morphology of the polymer and on the microphase separation phenomenon that occurs during different stages of shape memory cycling.

SAXS patterns and intensity distributions are dependent on the shape, size, and size distribution of the scattering objects. Thus, this technique is suitable for studying the structure of mass fractal aggregates, including primary particles. The angular dependence of the scattering vector is mainly determined by the size of the colloidal particles, their tendency to aggregate, the porosity of the disperse system, and the magnitude of the specific surface area [36].

Figure 6 illustrates 2D SAXS patterns of PU-I, PU-II, and PU-III for three conditions: (a) the undeformed condition, (b) Step 3, and (c) Step 4, as illustrated in Scheme 2. Two maxima are observed occurring along the stretching direction on both sides of the beam stopper for PU-II and PU-III. The maxima are due to scattering from the oriented structure. The patterns indicate a high degree of orientation obtained from the deformation process [37]. During Step 4 of the shape memory cycle, the PU patterns show recovery of the original nonoriented structure.

Figure 7 illustrates the SAXS data of PU-I, PU-II, and PU-III as a function of the scattering vector, q. The samples were studied under the same three conditions: (a) the undeformed condition, (b) Step 3, and (c) Step 4. In order to allow for direct comparison between the curves, the PU-III data were divided by a factor of 10.

The scattering peak observed in the SAXS data of PU-II and PU-III arises due to local heterogeneities in the electron density of the materials, and it is usually interpreted as a consequence of the presence of distinct microphases with different electronic densities [36, 38, 39].

PU-II and PU-III were designed as three-phase structures, including an amorphous matrix, hard domains, and crystals. In order to discuss the phase separation, it is convenient to employ the Lorentz correction, the invariant quantity, Q_{inv}, which describes the electron density fluctuation of the polymer and is a good approximation for estimating the overall degree of phase separation in segmented polymers [38]. Q_{inv} can be obtained by integrating $I_{(q)}q^2$ over the range of scattering angles, as given in Eq. 7 [36, 38, 39].

$$Q_{inv} = \int_0^\infty I_{(q)}q^2 \, \mathrm{d}q \qquad (7)$$

Since Eq. 8 cannot be applied to the overall data of PU-II and PU-III during Step 3, due to the anisotropic orientation of the lamellae in the samples [37], the contributions of each phase to the Lorentz corrected SAXS patterns were separated by a deconvolution procedure. Gaussian curves were used to describe the scattering phenomena due to each phase. As predicted by the DSC results, the phases that are responsible for the observed X-ray scattering were: crystallites in soft domains, hard domains, and the amorphous matrix. As Q_{inv} is obtained by integrating $I_{(q)}q^2$ over the range of scattering angles, phases with higher electronic densities achieve higher integrated values; hence, the deconvoluted crystalline phase was associated with the phase with higher intensity values. The experimental results and the deconvoluted separated curves of PU-II during (a) the undeformed condition, (b) Step 3, and (c) Step 4 are given in Fig. 8a. The same procedure was adopted for PU-III, as shown in Fig. 8b.

Q_{inv} of each phase was obtained as a fraction of the total area. Figure 9 describes the three-phase structures of PU-II and PU-III during the shape memory cycle. Table 4 summarizes the results.

The deconvoluted SAXS results of the undeformed specimens predict that the structures of PU-II and PU-III are semi-crystalline and that the crystalline fraction follows the order of PU-I < PU-II < PU-III. Furthermore, the SAXS results predict that the degree of phase separation

Fig. 6 Small-angle X-ray scattering patterns of PU-I, PU-II, and PU-III during three stages: **a** undeformed condition, **b** Step 3, and **c** Step 4
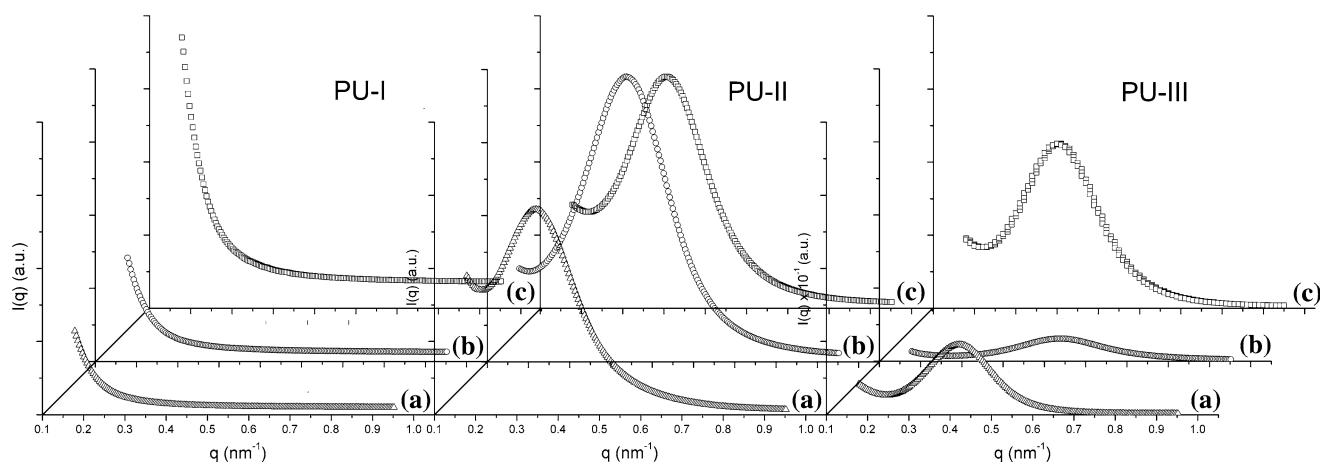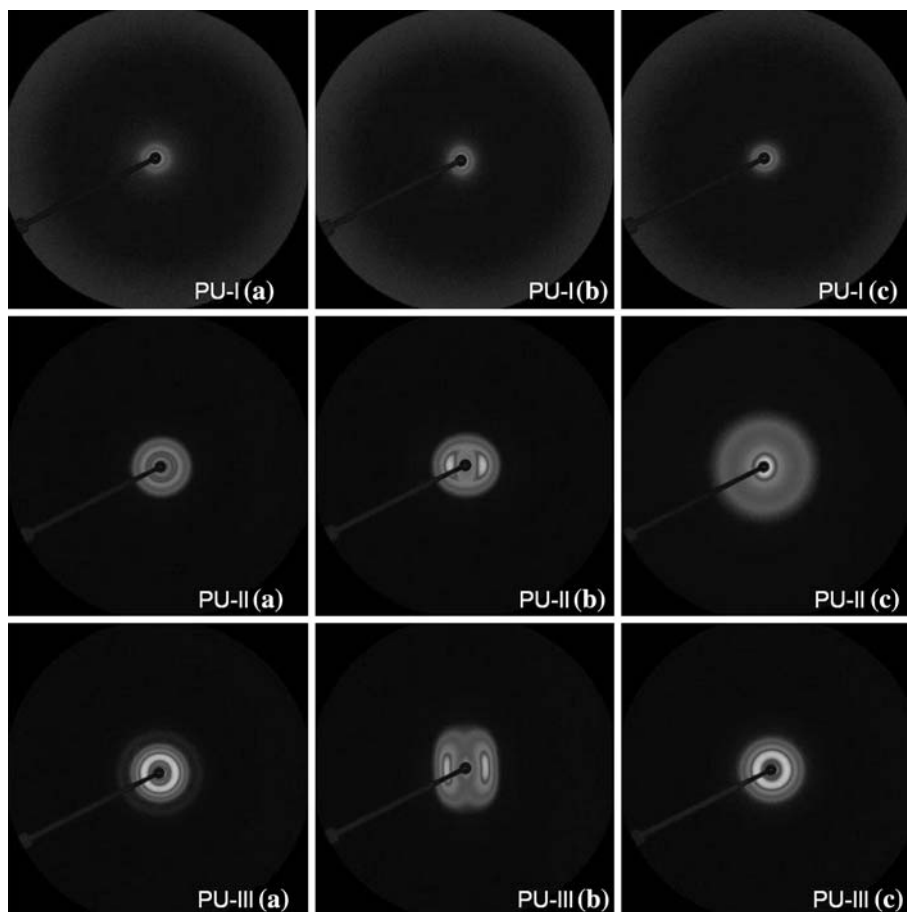

Fig. 7 SAXS curves for poly(ester–urethane) samples during different stages of the shape memory cycle: **a** undeformed specimens, **b** Step 3, and **c** Step 4

follows the order of PU-I < PU-II < PU-III, in accord with the WAXS and DSC results, suggesting that this method is capable of providing information about the polymer morphology.

The inter-domain repeat distance, L_{domain}, or the lamellar crystalline repeat distance, $L_{Crystal}$, depends on the molecular length of the polyester soft segment and the number and size of the hard domains as well as on the lamellar crystalline structure. L can be estimated from the q_{max} value corresponding to the maximum of the $I_{(q)}q^2$ versus q curve using Bragg's equation, Eq. 8 [36, 38, 39].
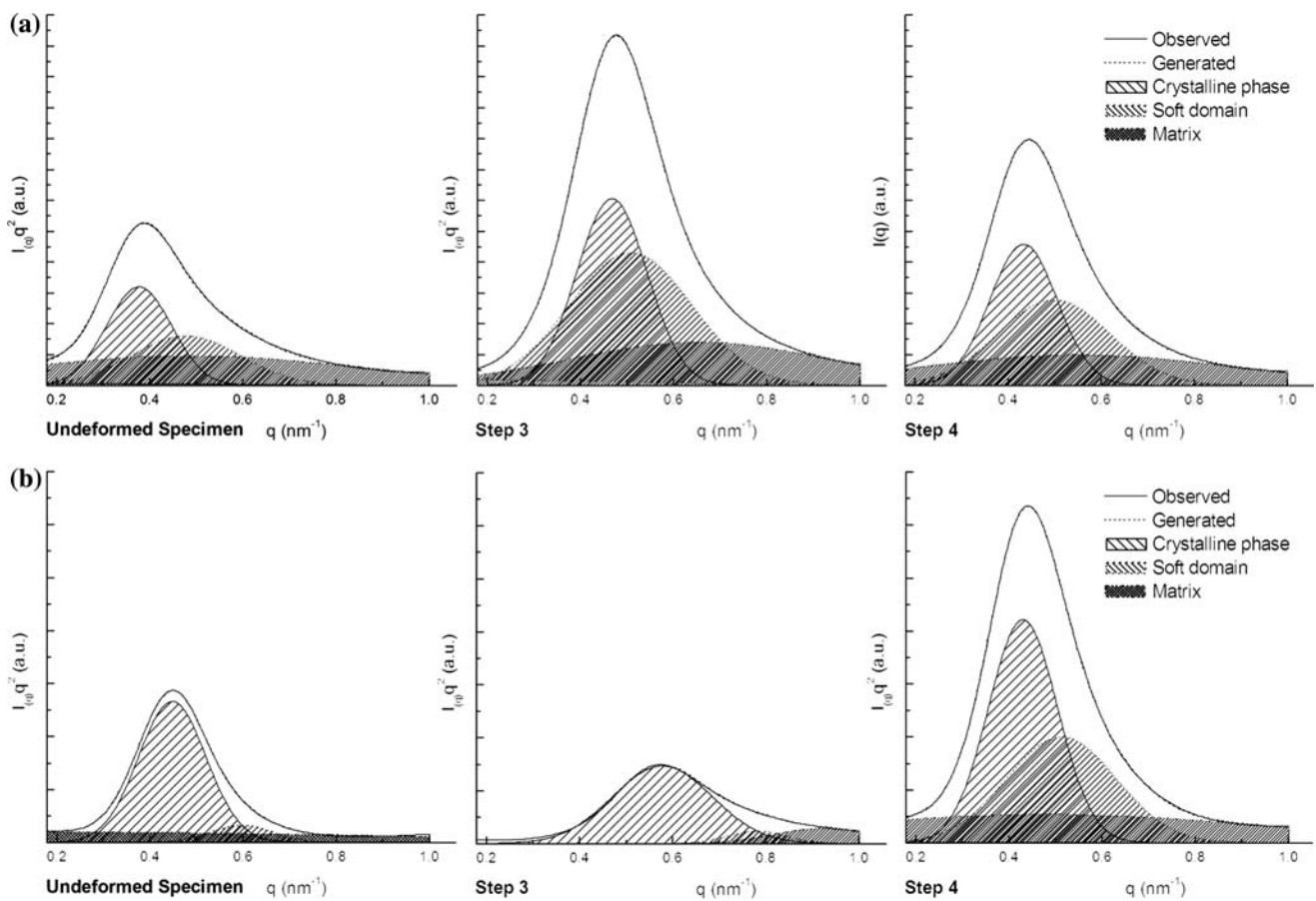
$$L = \frac{2\pi}{q_{max}} \tag{8}$$

Fig. 8 Deconvoluted Lorentz SAXS patterns of the samples **a** PU-II and **b** PU-III
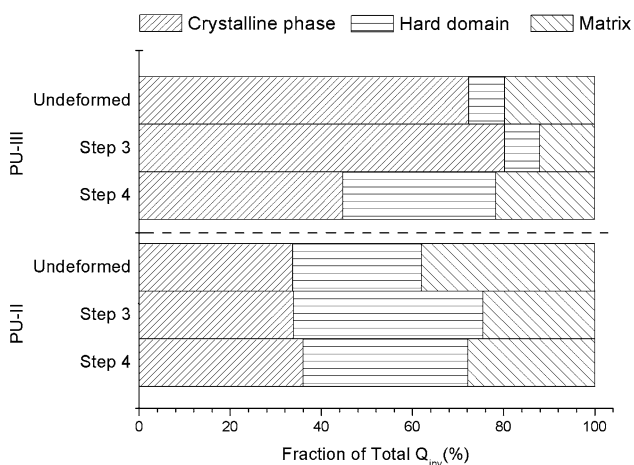

Fig. 9 PU-II and PU-III obtained three-phase structures during the shape memory cycle

Figure 10 describes the inter-domain repeat distance and the lamellar crystalline repeat distance of PU-II and PU-III during the shape memory cycle, derived from the

Table 4 Deconvoluted SAXS results of the crystalline phase, the hard domains, and the amorphous matrix as a fraction of the total Q_{inv}

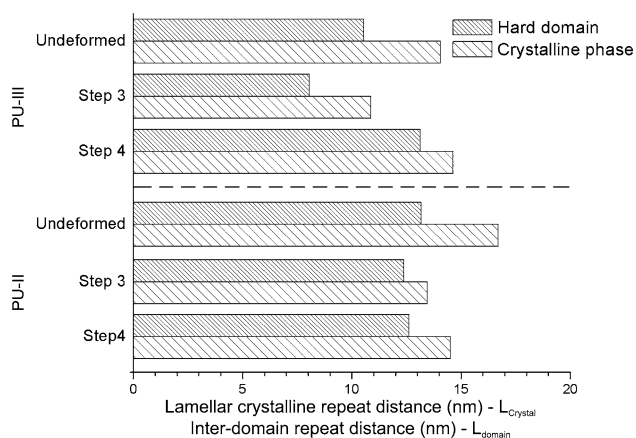|	Undeformed	Step 3	Step 4
PU-II			
Disperse phase			
Crystalline phase	33.7%	33.9%	36.1%
Hard Domain	28.3%	41.6%	36.1%
Matrix	38.0%	24.5%	27.8%
PU-III			
Disperse phase			
Crystalline phase	72.4%	80.3%	44.8%
Hard domain	7.9%	7.7%	33.6%
Matrix	19.7%	12.0%	21.7%
Matrix/Disperse phase ratio			
PU-II	0.61	0.32	0.39
PU-III	0.25	0.14	0.28
Hard domain/Crystalline phase ratio			
PU-II	0.84	1.23	1.00
PU-III	0.11	0.10	0.75

Fig. 10 Inter-domain repeat distance and lamellar crystalline repeat distance of PU-II and PU-III during the shape memory cycle
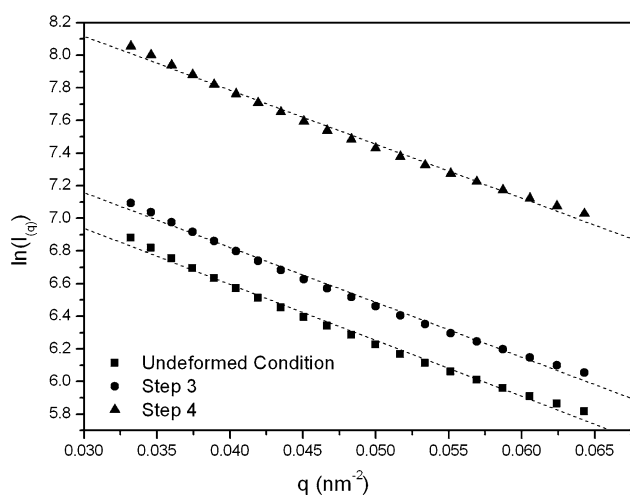

Fig. 11 SAXS experimental data and tangents of the PU-I experimental curve

deconvoluted curves in Fig. 10. Variations in the repeat distances observed in Fig. 10 may be related to the proportion of the phases determined in Fig. 11, i.e., phases with high contents display shorter inter-domain and/or inter-crystallite distances. Previous results [38, 39] have reported similar inter-lamellar repeated distances, varying from 12 to 16 nm.

The shape memory cycle induces changes in the phase proportion. Deformation promotes crystallization and phase separation. Recovery, however, did not appreciably modify the PU-II structure. The presence of PCL530 in the soft segments can restrict the chain packing efficiency, resulting in the formation of a less perfect crystal structure.

In SMPs, the relative motion and rearrangement of molecular chains are the primary mechanisms responsible for the shape-memory effect. The establishment and the annihilation of a metastable structure store and recover the deformation during the SM cycle [8, 9]. In the study,

the metastable structure formed during deformation stores the temporary shape in a stable manner and provides a lower entropy storage mechanism to the system. To recover the initial shape, melting of the disperse crystallites and re-distribution of the hard and soft segments into hard and soft domains provide enough freedom for the individual chains to move toward their initial positions.

Figures 6 and 7 indicate that there is a relationship between the ability of the studied PUs to recover their original shape after a sequence of thermo-mechanical treatments (which will be discussed later) and the ability to recover their original nanostructure. It can be seen that this ability to recover the original nanostructure is less pronounced in PU-II because PU-II did not have enough driving force to guide the system to restore its original structure after being deformed. This observation correlates well with the results obtained by measuring the shape memory properties of the samples, as will be reported later. Figure 9 indicates that the PU-III disperse phase, consisting of hard domains and crystalline phases, can more efficiently remember the initial disperse phase because the ratio between the matrix and the disperse phase does not significantly change after the shape memory cycle, even though the shape recovery brings major changes to the PU-III ratio between the hard domains and the crystalline phase (Table 4). Thereby, PUIII is more efficient in recovering its original shape, indicating that recovery is not only related to the composition of the disperse phase but also to its ability to reorganize during entropic recovery to more stable energy stages. Unlike PU-II, deformation promotes the crystallization of soft segments. During recovery, the crystals melt and enrich the matrix phase with soft segments. As a consequence, in the matrix bulk, the repulsive interaction between the dissimilar hard and soft segments increases, increasing their immiscibility and leading to hard domain segregation. This is not observed for PU-II mainly due to its different crystal structure, in which the presence of PCL530 soft segments reduces the polymeric chain's ability to rearrange.

As predicted by the FTIR results, due to the soft segment macromolecular architecture of PU-I (HBI(%) and W(HS)), a high degree of phase mixing between the hard and soft segments was observed. Therefore, the scattering intensity of PU-I shown in Fig. 10 decreases monotonically with q. The monotonically decreasing profile of PU-I is similar to the Guinier plot for an isolated domain system at very high dilution [36, 40]. In this case, the particulate system is made up of many particles with different sizes. This results in the experimental curve departing from linearity and becoming concave at higher values of q. The size of the dispersion particles can be calculated by Guinier's method if the distance between the particles is much larger than the particle size. In most cases, the shape of the particles is unknown [36].

By Guinier's method, the dependence of the SAXS intensity, $I_{(q)}$, on the scattering angle can be described by the following relationship, Eq. 9 [36].

$$I_{(q)} = I_e n^2 N \exp\left(-\frac{4\pi^2 \phi^2 R_o^2}{3\lambda^2}\right) = K_o \exp\left(-\frac{4\pi^2 \phi^2 R_o^2}{3\lambda^2}\right),$$

(9)

where I_e is the scattering intensity when the X-ray is subject to the scattering of a single electron, N is Avogadro's constant, n is the electron number of the scattering object, ϕ is the scattering angle, λ is the wavelength of the X-ray, and R_o is the radius of gyration of the dispersion system. For spherical particles, the radius of these particles (r) can be calculated from the following, Eq. 10 [36, 40]:

$$R_o = \sqrt{\frac{3}{5}} r.$$

(10)

A good approximation for evaluating r can be obtained by Eq. 11 [40]:

$$I_{(q)} \propto \exp\left(-\frac{R_o^2}{3} q^2\right).$$

(11)

Figure 11 shows typical Guinier plots, showing good straight lines, as expected from Eq. 13. From the slope of the straight line, one can calculate R_o.

The Q_{inv}, L_{domain}, $L_{Crystal}$, and r values for PU-I, PU-II, and PU-III for the undeformed condition, Step 3, and Step 4 are summarized in Table 6. Comparing the values of r for PU-I, it can be seen that the radius of the particles tends to decrease slightly during the shape memory cycle (Table 5).

Table 5 SAXS experimental data: Q_{inv}, $L_{Crystal}$, L_{domain}, and r

	$r_{average}$	Q_{inv}	L (nm)	
			Crystalline phase	Soft domain
Undeformed Condition				
PU-I	13.1	8.7	–	–
PU-II	–	82.8	16.8	13.2
PU-III	–	334.8	14.0	10.5
Step 3				
PU-I	13.0	9.8	–	–
PU-II	–	–	–	–
PU-III	–	–	–	–
Step 4				
PU-I	12.9	23.6	–	–
PU-II	–	115.5	14.5	12.6
PU-III	–	876.0	14.6	13.1

Mechanical and shape memory properties

Figure 12 shows typical stress–strain curves for PU-I, PU-II, and PU-III at room temperature, and Table 6 summarizes the mechanical properties, as well the corresponding shape memory properties.

PU-I and PU-II showed mechanical behavior typical of ductile polymers, with the presence of a clear yielding point. PU-III, however, showed behavior characteristic of a brittle polymer: no plastic deformation after the elastic strain.

It is clear that an increase in W(HS) produced an increase in modulus and in stress at yield. These results show that the mechanical properties of PUs are highly dependent on the hard-segment content, which agrees well with previous reports [24–26, 41]. Hard segments can bind themselves via hydrogen bonds, which results in an enhancement in the stiffness and strength of PUs.

The reversible phase was designed to actuate during the softening of the soft domains or during the melting of the crystallites. However, the R_r value of PUs is also highly dependent on the hard-segment content. Strong interactions among hard segments provide enough energy to restore the polymer back to its original shape. As reported previously [42], no clear relationship between W(HS) and R_r has been observed for PU copolymers. In fact, in order to achieve
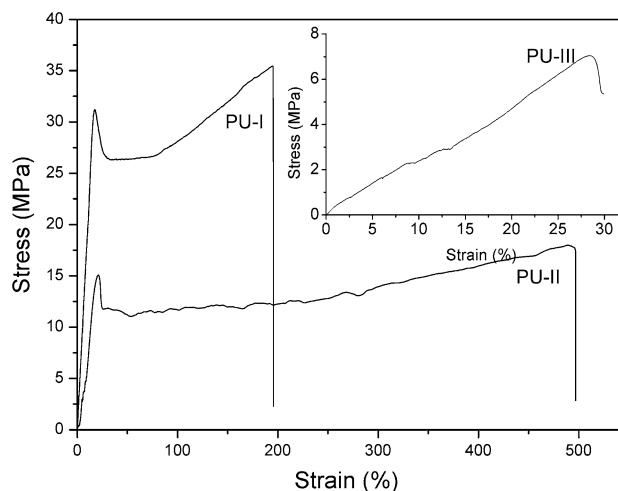

Fig. 12 Stress–strain curves of PU-I, PU-II, and PU-III

Table 6 Mechanical and shape memory properties of PU-I, PU-II, and PU-III

PU	σ_m (MPa)	ε_m (%)	E (MPa)	R_f (%)	R_r (%)
I	35	196	7	87	67
II	17	497	3	86	41
III	7	30	2	98	95

favorable SM properties, the polymer must have an optimal degree of fixed phase and reversible phase.

In PU-I, the presence of a high degree of hydrogen bonding between hard segments partially compensates its low index of crystallinity, yielding materials with R_r values close to 67%. This result suggests that hydrogen bonding is an important feature of shape memory PUs for both fixing and restoring shapes.

Even lower values of R_r were displayed by PU-II, which has low values of both hydrogen bonding and crystallinity. The presence of PCL530 within the soft segments containing PCL10000 restricts both crystallization of the soft segments and also disrupts the structure to reduce hydrogen bonding. These two factors are responsible for reducing the shape memory capacity of this sample (PU-II). On the other hand, a very high value for R_r was displayed by samples containing only PCL10000 as soft segments (PU-III), as a result of the combination of high degrees of both hydrogen bonding and crystallinity.

Conclusions

Shape memory poly(ester–urethane) samples with varying hard-segment contents and degrees of phase separation were synthesized. The hard-segment content controls the thermal, mechanical, and morphological properties. SAXS results showed that the ability of a specimen to recover its shape is related to the ability of specific macromolecular architectures to have their nanostructure rebuilt after the shape memory cycle. Shape memory properties were driven by the disperse phase: the deformed disperse phase stores the deformed shape; the melting of the disperse phase recovers the initial shape. For the PUs obtained, hydrogen bonding and crystal packing influence the disperse phase and, therefore, regulate the shape memory properties.

References

1. Szycher M (1999) Szycher's handbook of polyurethanes, chap 1.1–1.6. CRC Press, London
2. Oertel G (1994) Polyurethane handbook, 2nd edn. Hanser Publisher, New York, pp 11–45
3. Pan H, Chen D (2007) Eur Polym J 43:3766
4. Chen G, Ma Y, Zheng X et al (2007) J Polym Sci B 45(6):654
5. Lendlein A, Langer R (2002) Science 296(5573):1673
6. Wilson TS, Small W, Benett WJ et al (2005) In: Proc SPIE Int Soc Opt Eng, 60070R-1-8
7. Miaudet P, Derre A, Maugey M et al (2007) Science 318:1294
8. Gall K, Dunn ML, Liu YP, Stefanic G, Balzar (2004) Appl Polym Sci 85(2):290
9. Gall K, Kreiner P, Turner D, Hulse M (2004) J Micro Sys 13(3):472
10. Van Krevelen DW (1990) Properties of polymers, 3rd edn. Elsevier Science, Amsterdam, p 121
11. Oliveira W, Glasser WG (1994) Macromolecules 27:5
12. Bao H, Zhang Z, Ying S (1996) Polymer 37(13):2751
13. Seymour RW, Cooper RL (1973) Macromolecules 6:48
14. Gunes IS, Jana SC (2008) J Nanosci Nanotechnol 8(4):1616
15. Gorna K, Gogolewski S (2002) Polym Degrad Stab 75(1):113
16. Yeganeh H, Lakouraj MM, Jamshidi S (2005) Eur Polym J 41(10):2370
17. Jiang X, Li JH, Ding MM et al (2007) Eur Polym J 43(5):1838
18. Ayres E, Oréfice RL, Yoshida MI (2007) Eur Polym J 43(8):3510
19. Coates JP (2000) In: Meyers RA (ed) Encyclopedia of analytical chemistry. Wiley, Chichester, UK, pp 10815–10837
20. Marcos-Fernández A, Abraham GA, Valentín JL, San Román J (2006) Polymer 47(3):785
21. Chattopadhyay DK, Sreedhar B, Raju KVSN (2006) Polymer 47(11):3814
22. Cho JW, Lee SH (2004) Eur Polym J 40(7):1343
23. Huang SL, Lai JY (1997) Eur Polym J 33(10–12):1563
24. Liu Y, Pan C (1998) Eur Polym J 34(5–6):621
25. Nakamae K, Nishino T, Asaoka S et al (1999) Int J Adhes Adhes 19(5):345
26. Pompe G, Pohlers A, Pötschke P, Pionteck J (1998) Polymer 39(21):5147
27. Lin JR, Chen LW (1998) J Appl Polym Sci 69(8):1563
28. Li YJ, Gao T, Liu J et al (1992) Macromolecules 25(26):7365
29. Pretsch T, Jakob I, Werner M (2009) Polym Degrad Stab 94:61
30. Tien YI, Wei KH (2001) Polymer 42(7):3213
31. Jia QM, Zheng M, Zhu YC et al (2007) Eur Polym J 43(1):35
32. Kim BK, Lee SY, Xu M (1996) Polymer 37(26):5781
33. Xu J, Shi W, Pang W (2006) Polymer 47(1):457
34. Charnetskaya AG, Polizos G, Shtompel VI et al (2003) Eur Polym J 39(11):2167
35. Wang ZG, Hsiao BS, Fu BX et al (2000) Polymer 41(5):1791
36. Wang SH, Zhang Y, Ren WT et al (2005) Polym Test 24(6):766
37. Jiang ZY, Tang YJ, Men YF et al (2007) Macromolecules 40(20):7263
38. Chang SL, Yu TL, Huang CC, Chen WC, Linliu K, Lin TL (1998) Polymer 39(15):3479
39. Li YJ, Kang WX, Stoffer JO et al (1994) Macromolecules 27(2):612
40. Tang YJ, Jiang ZY, Men YF et al (2007) Polymer 48(17):5125
41. Lee BS, Chun BC, Chung YC et al (2001) Macromolecules 34(18):6431
42. Yang JH, Chun BC, Chung YC, Cho JH (2003) Polymer 44(11):3